ACS AuthorChoice

Research Article

Li-Ion Diffusion in Nanoconfined LiBH$_4$-LiI/Al$_2$O$_3$: From 2D Bulk Transport to 3D Long-Range Interfacial Dynamics

Roman Zettl,* Maria Gombotz, David Clarkson, Steven G. Greenbaum, Peter Ngene, Petra E. de Jongh, and H. Martin R. Wilkening*

Cite This: *ACS Appl. Mater. Interfaces* 2020, 12, 38570−38583

Read Online

ACCESS | Metrics & More | Article Recommendations | Supporting Information

ABSTRACT: Solid electrolytes based on LiBH$_4$ receive much attention because of their high ionic conductivity, electrochemical robustness, and low interfacial resistance against Li metal. The highly conductive hexagonal modification of LiBH$_4$ can be stabilized via the incorporation of LiI. If the resulting LiBH$_4$-LiI is confined to the nanopores of an oxide, such as Al$_2$O$_3$, interface-engineered LiBH$_4$-LiI/Al$_2$O$_3$ is obtained that revealed promising properties as a solid electrolyte. The underlying principles of Li$^+$ conduction in such a nanocomposite are, however, far from being understood completely. Here, we used broadband conductivity spectroscopy and ^{1}H, ^{6}Li, ^{7}Li, ^{11}B, and ^{27}Al nuclear magnetic resonance (NMR) to study structural and dynamic features of nanoconfined LiBH$_4$-LiI/Al$_2$O$_3$. In particular, diffusion-induced ^{1}H, ^{7}Li, and ^{11}B NMR spin−lattice relaxation measurements and ^{7}Li-pulsed field gradient (PFG) NMR experiments were used to extract activation energies and diffusion coefficients. ^{27}Al magic angle spinning NMR revealed surface interactions of LiBH$_4$-LiI with pentacoordinated Al sites, and two-component ^{1}H NMR line shapes clearly revealed heterogeneous dynamic processes. These results show that interfacial regions have a determining influence on overall ionic transport (0.1 mS cm^{-1} at 293 K). Importantly, electrical relaxation in the LiBH$_4$-LiI regions turned out to be fully homogenous. This view is supported by ^{7}Li NMR results, which can be interpreted with an overall (averaged) spin ensemble subjected to uniform dipolar magnetic and quadrupolar electric interactions. Finally, broadband conductivity spectroscopy gives strong evidence for 2D ionic transport in the LiBH$_4$-LiI bulk regions which we observed over a dynamic range of 8 orders of magnitude. Macroscopic diffusion coefficients from PFG NMR agree with those estimated from measurements of ionic conductivity and nuclear spin relaxation. The resulting 3D ionic transport in nanoconfined LiBH$_4$-LiI/Al$_2$O$_3$ is characterized by an activation energy of 0.43 eV.
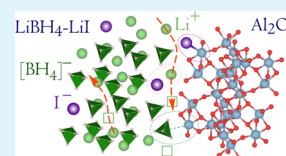
KEYWORDS: lithium borohydride, nanoconfinement, electrolytes, dynamics, conductivity, NMR

1. INTRODUCTION

The increase of anthropogenic CO$_2$ in the atmosphere is responsible for the global warming observed; this warming is generally known as the greenhouse effect. Burning of fossil fuels belongs to one of the main sources of energy-related CO$_2$ emissions. Cutting our dependency on hydrocarbons, such as coal, fuel oil, or natural gas, and finding alternatives to convert energy, e.g., from solar or wind power, to electricity is one of the most important challenges that humans need to face within the 21st century. As electricity from solar power is generated from a nondispatchable source of energy and, thus, highly intermittent, we have to develop high-performance and sustainable energy storage devices that are connected to the electricity grid in a mainly decentralized way.[1] Secondary batteries, which either use Li$^+$ or Na$^+$ ions as ionic charge carriers, are suitable devices for this purpose.[2−5] While Na-based batteries are envisaged to play a pivotal role in stationary energy storage,[5] Li$^+$-ion batteries offering both considerably higher energy densities and higher power densities are the devices of choice for automotive applications.[3,6] Currently, these systems use flammable, aprotic liquid electrolytes. To increase both safety and longevity, solid electrolytes attracted great attention. Highly conducting solids, that is, polymers or

ceramics, are at the heart of all-solid-state systems as they ensure the facile transport of the ions between the two compartments of a battery, viz., the anode and cathode.[4,7−9]

Over the last years, many ceramic materials that show ionic conductivities with values reaching or even exceeding a benchmark of 1 mS cm^{-1} have been presented.[7,9,10] Each material, regardless of whether being an oxide, sulfide, thiophosphate, or hydride, has its own advantages and disadvantages with respect to, for example, electrochemical stability, interfacial resistance, chemical robustness, synthesis costs, and sustainability.[7]

Highly conducting anion-substituted hydrides based on lithium borohydride (LiBH$_4$) especially when prepared in nanostructured forms that benefit from interfacial properties belong to the core group of sustainable materials composed of elements with high natural abundance. Quite recently, some of
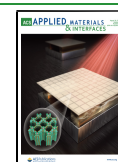
us reported on enhanced ion dynamics in nanoconfined LiBH$_4$-LiI.[11] Nanoconfinement was achieved by melt infiltration of LiBH$_4$-LiI in the nanopores of alumina, Al$_2$O$_3$. The combination of both (i) substitutions of iodide anions for the BH$_4^-$ units and (ii) spatial confinement resulted in a composite material with promising ion conductivities at room temperature. The underlying transport mechanism in this interface-controlled or surface-dominated material remains, however, unclear. Here, we used time domain and magic angle spinning (MAS) nuclear magnetic resonance (NMR) spectroscopy to shed light on both structural features and ion dynamics in nanoconfined LiBH$_4$-LiI.

Numerous publications, which appeared over the last decades, pointed out that various NMR techniques represent crucial and powerful analysis methods also in metal hydrides research. Already in 1987, Jarrett et al.[12] used solid-state ^{2}H NMR to identify bridging and terminal metal hydride sites. In LiZn$_2$(BD$_4$)$_5$ ^{11}B MAS NMR and multiple quantum MAS NMR helped identify four different boron sites in the [Zn$_2$(BD$_4$)$_5$]$^-$ anion.[13] Furthermore, ^{1}H, ^{7}Li, and ^{11}B NMR, including spin–lattice relaxation rate measurements in particular, were used to characterize the translational and rotational dynamics in this compound.[14]

Before complex metal hydrides received considerable attention from the battery research community, lithium borohydride, LiBH$_4$, and its relatives were intensively investigated as hydrogen storage materials;[15−18] NMR played a central role in characterizing both local structures and ion dynamics.[19,20] As an example, Mg(BH$_4$)$_2$(NH$_3$BH$_3$)$_2$, that is, a metal borohydride–ammonia borane complex, was proposed as a good candidate for hydrogen storage. Results from ^{11}B MAS NMR were compared with those from DFT calculations to validate the crystal structure.[21] It turned out that the excellent hydrogen-sorption properties found could be further enhanced by synthesizing composites with nanoscaffolds.[22−24] Gutowska et al.[25] used solid-state ^{11}B NMR to underline their hypothesis that nanoconfinement of the complex metal hydrides decreases the temperature for hydrogen release from ammonia borane together with an increase in hydrogen purity. Conradi and co-workers[26,27] presented an elegant NMR-based study using ^{1}H NMR and ^{7}Li NMR on LiBH$_4$ and LiBH$_4$ confined in carbon aerogel. They observed pronounced changes in Li mobility when going from bulk materials to nanoconfined samples.

Nanoconfinement is, in general, an elegant approach to increase the room-temperature conductivity of LiBH$_4$.[28−31] Bulk LiBH$_4$ undergoes a reversible structural change at approximately T_{pt} = 110 °C and changes from the highly conductive hexagonal phase to the poorly conductive orthorhombic phase.[32] The scaffolds of the nanoconfined complex hydrides are ionic insulators. In such conductor/insulator composites,[33−37] enhanced ion transport along the heterointerfaces can occur due to both structural disorder[38−40] and/or space charge effects.[35,41−43]

The first NMR studies on LiBH$_4$, which was confined in silica, were realized in 2012 by Kentgens and co-workers.[44] In the following years, solid-state NMR, especially ^{7}Li NMR, proved itself as a powerful technique to study Li diffusion in these compounds that were envisaged as solid electrolytes for Li batteries.[28,29,45] Quite recently, the same group[46] reported on the phase behavior and Li ion dynamics of nanoconfined LiBH$_4$ in silica. Furthermore, the second approach to increase ionic conductivity, which is anion substitution with, e.g., LiI

(vide supra), was successfully studied via solid-state NMR.[47,48] As mentioned above, replacing [BH$_4$]$^-$ partly by halogen anions such as I$^-$ stabilizes the highly conducting hexagonal phase of LiBH$_4$ at room temperature.

Despite the various studies,[26,28−31,46] the role of the interface of the pore walls and complex hydride is not completely clear yet. A reaction or at least an interaction of the surface groups of the porous supports (Al$_2$O$_3$ or SiO$_2$) with the metal hydride could be the key factor to explain the origin of the significant increase in ionic conduction upon nanoconfinement. Most of these studies deal with silica supports. It was, however, shown that the surface groups in alumina beneficially affected ion diffusion too;[36] similar effects were found with other oxides such as MgO, CaO, TiO$_2$, and ZrO$_2$.[49] These surface groups can, in ideal cases, be identified via ^{27}Al MAS NMR. Besides the well-known NMR signals for octahedrally and tetrahedrally coordinated Al in nanostructured γ-Al$_2$O$_3$, another signal shows up. In terms of chemical shift values, this signal is located between these two main signals and points to pentacoordinated alumina near the surface regions.[50−52] Such sites might be involved in ion transport in nanoconfined, anion-stabilized LiBH$_4$-LiI/Al$_2$O$_3$.

In our recent study on this system,[11] we shed light on the correlation between morphology and Li-ion conductivity by means of X-ray diffraction, diffuse reflectance infrared Fourier transform spectra, N$_2$ physisorption, and scanning electron microscopy. Impedance spectroscopy was used to characterize long-range ion transport in the nanoconfined composite. The present paper is aimed at giving insights into the mechanisms of Li$^+$ diffusion in LiBH$_4$-LiI/Al$_2$O$_3$. For this purpose, we used solid-state NMR techniques including variable-temperature ^{1}H, ^{7}Li, and ^{11}B spin–lattice relaxation measurements and ^{7}Li pulsed-field gradient (PFG) experiments to study ion dynamics on different length scales. We compare our results with transport parameters extracted from broadband conductivity measurements and electrical modulus spectroscopy. Structural features of the sample were probed by ^{1}H, ^{6}Li, ^{11}B, and ^{27}Al MAS NMR. Taken together, we show that nuclear spin relaxation, PFG NMR, and electrical relaxation provide consistent diffusion coefficients characterizing long-range ion dynamics. Via the combination of these techniques, we were able to study ion transport in the nanoconfined ion conductor over a dynamic range of 6−8 orders of magnitude.

2. EXPERIMENTAL SECTION

2.1. Preparation of the LiBH$_4$-LiI/Al$_2$O$_3$ Electrolyte. Lithium boron hydride (LiBH$_4$, with a purity of 95%, Sigma Aldrich) and lithium iodide (LiI, 98%, Sigma Aldrich) were thoroughly mixed for several minutes in a ceramic mortar. The molar ratio LiBH$_4$/LiI was 80:20. A sufficient amount of physical mixture was added to the porous support material, alumina (Al$_2$O$_3$, Sasol Puralox SCCa-5/200, see ref 11 for detail), to fill the pores by 130%. The pore size was determined by N$_2$ physisorption and turned out to be 8.7 nm.[11] The extra 30% was added to enable interconnectivity between the insulating alumina particles. The calculation was done after the specific pore volume has been determined via N$_2$ physisorption. To finally obtain the melt-infiltrated alumina product, the mixture was filled in a quartz reactor and placed inside a stainless-steel high-pressure autoclave (Parr). After applying a pressure of 50 bar H$_2$, the sample was heated to ϑ = 295 °C with a heating rate of approximately 3 °C min^{-1}. During a dwell time of 30 min, LiBH$_4$ and LiI built a solid solution and infiltrate the pores of the alumina support.[53] For a more detailed description, we refer to our recent study,[11] which also includes the characterization of the reference samples LiBH$_4$-LiI, i.e., a sample without alumina.
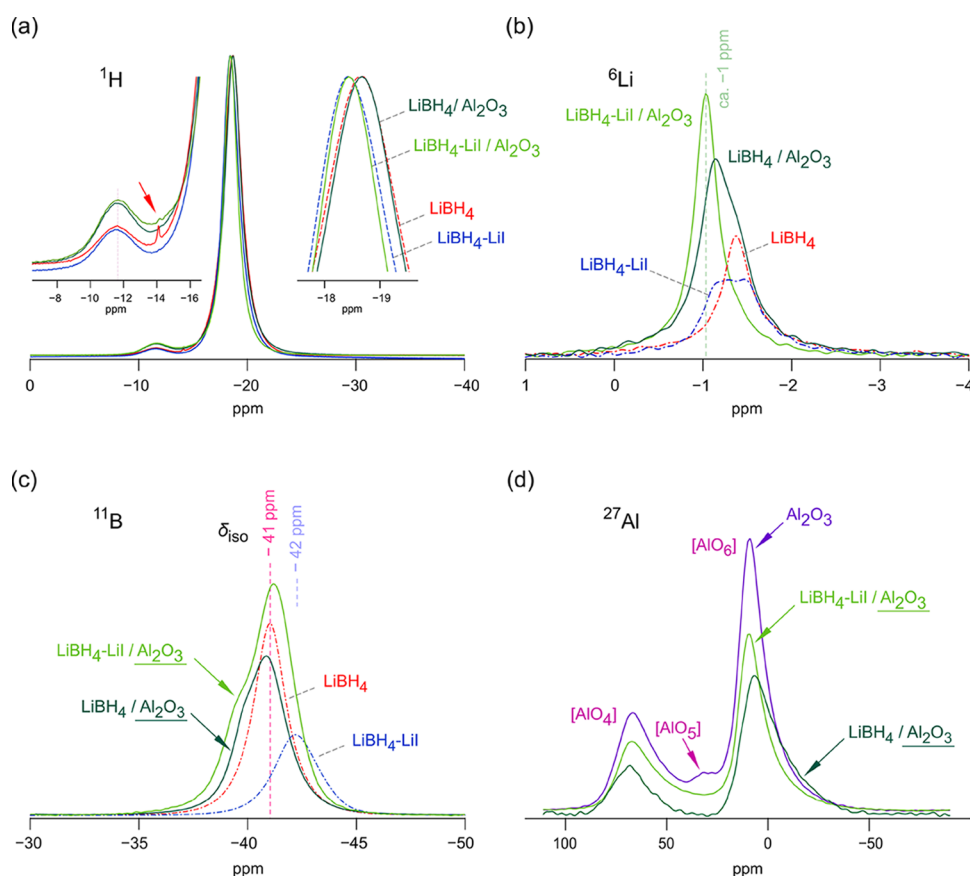
Figure 1. ^1H, ^6Li, ^{11}B, and ^{27}Al MAS NMR spectra of $LiBH_4$-LiI/Al_2O_3, the NMR spectra are compared with those of $LiBH_4$, $LiBH_4$-LiI, $LiBH_4/Al_2O_3$, and Al_2O_3, respectively. The spinning speed was 25 kHz. (a) ^1H MAS NMR spectra, most likely, the small arrow indicates an impurity phase. (b) ^6Li MAS NMR spectra, for $LiBH_4/Al_2O_3$, a line composed of two spectral components is observed. (c) ^{11}B MAS NMR spectra, which also show a two-component line shape for the nanoconfined samples. (d) ^{27}Al MAS NMR spectra of Al_2O_3, besides lines attributable to four- and six-fold Al species, we also recognize pentacoordinated Al centers, $[AlO_5]$. Most likely, as this signal does not show up in the spectra of $LiBH_4/Al_2O_3$ and $LiBH_4$-LiI/Al_2O_3, we assume that six-fold coordinated surface species $[AlO_5X]$ (X = I, BH_4^-) have been formed.

2.2. Nuclear Magnetic Resonance. Samples for MAS NMR measurements were filled in Bruker MAS rotors (ZrO_2) with a diameter of 2.5 mm and a length of 1 cm. The rotors were carefully filled portion by portion with the powder sample, which was pressed by hand after each filling step to prepare a dense-packed rotor. Various reference samples such as $LiBH_4$, Al_2O_3, $LiBH_4$-LiI, and $LiBH_4/Al_2O_3$ were also investigated to interpret the results of the nanoconfined composite $LiBH_4$-LiI/Al_2O_3 obtained via ^1H, ^6Li, ^{11}B, and ^{27}Al MAS NMR. To acquire the spectra, we used a Bruker Avance III 500 spectrometer that was connected to an 11.4 Tesla cryomagnet. This magnet field corresponds to the following resonance frequencies: 500.00 MHz (^1H), 73.58 MHz (^6Li), 160.42 MHz (^{11}B), and 130.29 MHz (^{27}Al). The MAS probe was operated at a spinning speed of 25 kHz. The temperature of the bearing gas was set to approximately $\vartheta = 30\,°C$. Spectra were recorded with a single-pulse excitation sequence. Pulse lengths, delay times, and number of scans for each spectrum are listed in Table S1. Free induction decays were Fourier transformed to obtain spectra without any further manipulation except for zero- and first-order phase correction.

Information about ion dynamics, i.e., activation energies E_a, jump rates τ^{-1}, was collected under static, that is, under non-MAS conditions with a Bruker Avance III 300 spectrometer. The spectrometer was connected to a 7.0 Tesla cryomagnet yielding the following resonance frequencies for the nuclei under investigation: 300.00 MHz (^1H), 116.59 MHz (^7Li), and 96.25 MHz (^{11}B). $LiBH_4$-LiI/Al_2O_3 was fire-sealed in Duran tubes for the ^7Li and ^1H measurements and in quartz tubes for the ^{11}B experiments, respectively. The samples were placed in a commercially available probe head (Bruker) designed to be operated at temperatures ϑ as

high as 300 °C; the probe was equipped with a ceramic sample chamber and a type T thermocouple to monitor the temperature which we adjusted with a stream of nitrogen gas that passed a heater beneath the sample chamber. The heater was connected to a Eurotherm temperature controller. We varied the temperature for the measurements of longitudinal NMR spin−lattice relaxation (SLR) rates R_1 ($1/T_1$) and for the measurement of the spin-lock rates $R_{1\rho}$ ($1/T_{1\rho}$) from −100 °C to 160 °C.

The so-called saturation recovery pulse sequence was used to record the $1/T_1$ rates in the laboratory frame of reference: a comb of closely spaced $\pi/2$ pulses destroys any longitudinal magnetization M_z. The subsequent recovery curve of M_z, see the Supporting Information (Figure S1), is obtained by plotting the area under the free induction decays (FIDs) against the waiting time t_d. To parametrize the transients $M_z(t_d)$, stretched exponential fits were used, $M_z(t_d) \propto 1 - \exp(-(t_d/T_1)^\gamma)$ with $0 < \gamma \leq 1$. Rotating-frame ^7Li NMR SLRρ rates were acquired with the spin-lock technique at a locking frequency of 20 kHz. The spin-lock period t_{lock} was varied such that it takes values from 10 μs to 1 s. Worth noting, it is crucial to ensure full longitudinal relaxation between each spin-lock scan. This is realized by paying attention to a recycle delay of 5 × T_1. Again, stretched exponential fits were used to analyze the transversal transients, $M_\rho(t_{lock})$: $M_\rho(t_{lock}) \propto \exp(-(t_{lock}/T_{1\rho})^\varphi)$ with $0 < \varphi \leq 1$, see Figure S1, and obtain the $R_{1\rho}$ rates ($1/T_{1\rho}$). All sample preparation steps for MAS NMR and static NMR were carried out under a protective argon (Ar) atmosphere. Pulse lengths, delay times, and number of scans of the time-domain experiments are summarized in Table S1 also.

PFG diffusion-ordered spectroscopy (DOSY) NMR was conducted using a 300 MHz Varian direct drive spectrometer and Doty Scientific

closed-bore gradient probe capable of producing gradients of up to 1200 G cm^{-1}. The sample was packed under the Ar atmosphere into high-throughput NMR tubes (Wilmad) with a 5 mm outer diameter and sealed with tight-fitting caps and Parafilm. ^{7}Li NMR experiments were then conducted to determine the relaxation and diffusion properties of the sample at different temperatures. For further information on the PFG DOSY experiment, we refer to the Supporting Information section. Results were fit using the Stejskal–Tanner equation for stimulated echo pulse sequences with square pulses, see Figure S2 and the Supporting Information for details.

Transverse relaxation times T_2 were measured at three temperatures, viz., at 25, 60, and 90 °C using a Hahn–Echo pulse sequence with variable delays; corresponding transients are shown in Figure S3. At 25 °C, the spin–spin relaxation time was 500 μs. At 60 and 90 °C, T_2 increased, however, to 2.7 and 4.9 ms, respectively. T_1 was approximated to be on the order of hundreds of milliseconds at all temperatures based on sample saturation observation at shorter delays between single-pulse experiments. In fact, independent measurements of T_1 yielded T_1 = 590 ms at 60 °C (116.59 MHz) and T_1 = 510 ms at ϑ = 100 °C. This circumstance enabled sufficiently long diffusion times in ^{7}Li-stimulated echo DOSY experiments and the measurement of diffusion coefficients on the order of 10^{-12} m^2 s^{-1}. Diffusion coefficients were measured using a stimulated echo DOSY sequence with a longitudinal eddy current delay, varying the gradient strength between 0 and 650 G cm^{-1}. The attenuation curves measured and associated fits are presented in Figure S2.

2.3. Impedance Spectroscopy. For the impedance spectroscopy measurements, a sample of LiBH$_4$-LiI/Al$_2$O$_3$ was pelletized with a load of 0.5 tons. The final two pellets (5 mm in diameter) were sputtered on both sides with gold. The Au layers (100 nm in thickness) acted as ion-blocking electrodes. The sample was placed in an active ZGS sample cell (Novocontrol), which was connected to a Concept 80 broadband impedance spectrometer (Novocontrol) using an Alpha-A analyzer. The cell was continuously flushed with a stream of freshly evaporated nitrogen to avoid any contamination or reaction with moisture. The sample was placed between two gold-sputtered spacer electrodes and a spring to ensure a sufficiently long contact throughout the measurements. We corrected the measured impedance for the cell stray and spacer capacity, which depends on the dimensions of the electrodes and the sample pellet itself. Conductivity isotherms were recorded at temperatures ϑ ranging from −50 to 100 °C in a frequency range of 10 MHz to 10 mHz.

A second pellet of the same batch was used to carry out variable-temperature impedance measurements but at fixed frequencies of 100 Hz and 100 kHz (−140 to 160 °C, in steps of 5 °C). We analyzed the resistivity in the form of M''/ω where M'' is the imaginary part of the complex electric modulus, and ω denotes the angular frequency. Such a plot reveals peaks being similar to those seen in ^{7}Li NMR spin–lattice relaxation.

3. RESULTS AND DISCUSSION

3.1. Structural Elucidation. High-resolution (MAS) NMR was used to observe structural changes of the different LiBH$_4$-based composites. ^{1}H, ^{6}Li, ^{11}B, and ^{27}Al MAS NMR spectra are shown in Figure 1. Intensities are given in arbitrary units; the spectra are scaled such that it is easier to differentiate between the distinct spectral contributions. The ^{1}H MAS NMR spectrum (Figure 1a) of LiBH$_4$-LiI/Al$_2$O$_3$ reveals a main signal that is very similar to that of the LiBH$_4$-LiI sample. The spectra of the samples without LiI are shifted toward lower parts per million (ppm) values, that is, these lines are upfield or shielded. Obviously, because halides have a higher electro-negativity than the borohydride anion, ^{1}H in the direct neighborhood of I experiences, on average, a reduced electron density at its site, and it is therefore less magnetically shielded. Consequently, the corresponding lines appear in the downfield region, i.e., they are shifted toward the direction of positive ppm values. Interestingly, nanoconfinement of LiBH$_4$ (or

LiBH$_4$-LiI) in Al$_2$O$_3$ did not lead to a shift on the ppm scale of the corresponding NMR lines.

The small signal at more positive ppm values (isotropic shift δ_{iso} = −11.5 ppm, see Figure 1a) might be attributed to an H-containing impurity phase. This signal is anticipated to be related to the 95% purity of the sample. The same holds for the tiny line located at −14 ppm (see arrow), which we also assign to a slight amount of impurities in pristine LiBH$_4$.[54] Most likely, these lines arise from compounds such as Li$_2$B$_{10}$H$_{10}$ or Li$_2$B$_{12}$H$_{12}$. Alternatively, it has been suggested, at least for LiBH$_4$/SiO$_2$, that this line would be attributed to trapped H$_2$, which is released as a result of a surface reaction between BH$_4^-$ and the silanol groups at the surface of the oxide.[45,55]

Compared to ^{1}H, ^{6}Li MAS NMR revealed more distinct changes when going from LiBH$_4$ to the final anion-stabilized nanocomposite, see Figure 1b. Coarse-grained LiBH$_4$ shows a signal at approximately δ_{iso} = −1.35 ppm, the ^{6}Li NMR spectra are referenced to an aqueous solution of LiCl (0 ppm, crystalline lithium acetate served as a secondary reference). If in contact with Al$_2$O$_3$, we see that more than approximately 50% of the Li ions, as estimated via deconvolution of the spectrum with Gaussian functions, experiences an NMR line shift toward positive ppm values. The original line, being reduced in intensity, is still seen. This feature reveals the important effect of Al$_2$O$_3$ and its surface groups on the ^{6}Li NMR signal of the composite.

Adding LiI to LiBH$_4$ broadens the LiBH$_4$ signal and shifts its center of gravity slightly to less negative ppm values; the NMR line of LiBH$_4$-LiI appears at ca. −1.3 ppm (Figure 1b). Broadening of the line might be explained by site disorder introduced. For LiBH$_4$-LiI/Al$_2$O$_3$, a single line is seen at δ_{iso} = −1 ppm (see Figure 1b). This line and its position can be explained by two-accumulating effects. Obviously, the Li ions in nanoconfined LiBH$_4$-LiI/Al$_2$O$_3$ experience a magnetic environment, which is similar but not identical with that in LiBH$_4$ or LiBH$_4$-LiI. As indicated by the line of LiBH$_4$/Al$_2$O$_3$, a large amount of Li$^+$ ions is influenced by the presence of Al$_2$O$_3$. For LiBH$_4$-LiI/Al$_2$O$_3$, this feature is even more pronounced. Second, as has been seen in a recent study,[11] compared to both LiBH$_4$-Al$_2$O$_3$ and LiBH$_4$-LiI, ion dynamics, and thus the Li$^+$ exchange rate, is noticeably higher in the nanoconfined composite. Hence, at room temperature, and above, the line already represents a motionally narrowed signal with the Li$^+$ ions experiencing a magnetically homogeneous matrix (see also below). This view is supported by variable-temperature ^{7}Li NMR line shape measurements revealing, from a dynamic point of view, a single, motionally narrowed central line. Moreover, the ^{7}Li NMR lines do only reveal a single-electric quadrupole pattern pointing to an ensemble of Li ions experiencing the same electric field gradient. This observation is in line with a magnetically homogeneous environment to which the single ^{6}Li MAS NMR line points.

For ^{11}B, we observed a single line for LiBH$_4$; the same is true for the line belonging to LiBH$_4$-LiI, which is shifted toward lower ppm values (see Figure 1c). The spectra were referenced to LiBH$_4$ whose signal shows up at −41 ppm when referenced to BF$_3$·O(CH$_2$CH$_3$)$_2$ (0 ppm), see Hwang et al.[56] While for the nonconfined samples, single lines are seen; those of the nanoconfined samples reveal two spectral components. For LiBH$_4$-LiI/Al$_2$O$_3$, we see that the original line, assigned to LiBH$_4$, is slightly shifted toward the position of the line of LiBH$_4$-LiI. In addition, a shoulder appeared that is also visible in the spectrum of LiBH$_4$/Al$_2$O$_3$ (Figure 1c). Most likely, ^{11}B
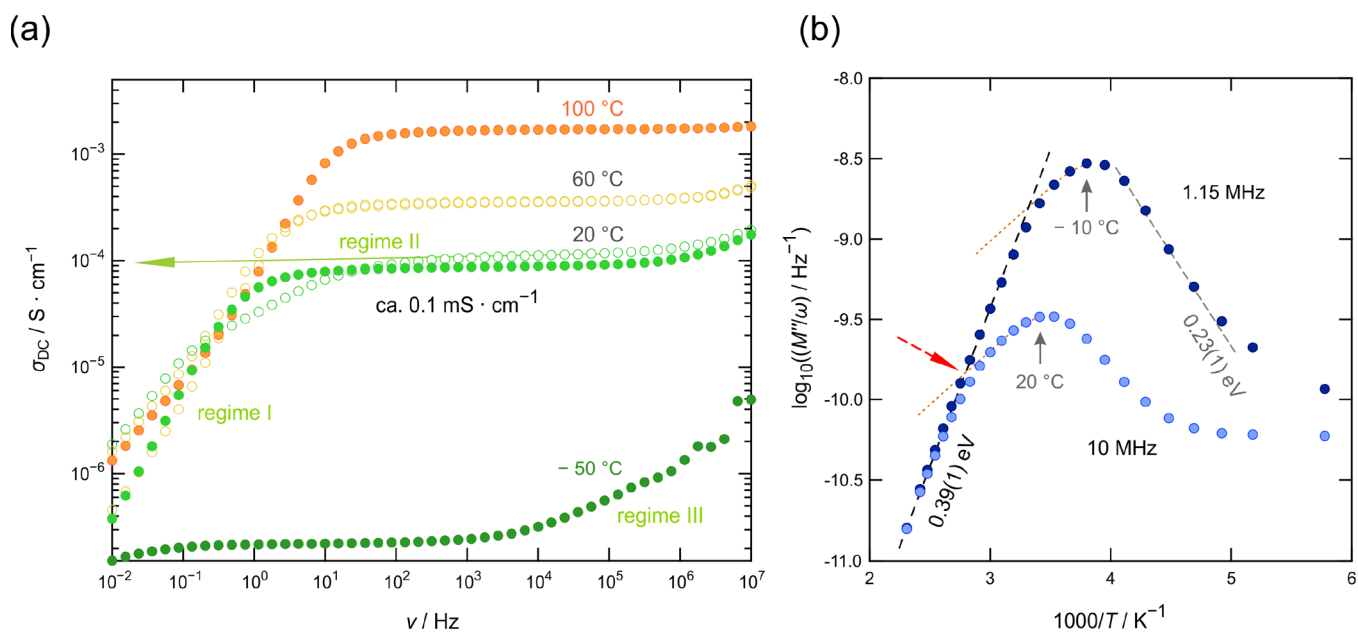
(a)

(b)

Figure 2. (a) Conductivity isotherms of nanoconfined $LiBH_4$-LiI/Al_2O_3 recorded at the temperatures indicated (pellet 1, the results of a second pellet are shown in Figure 4) with duplicate measurements at 20 and 60 °C, proving the temperature stability of the sample with respect to ionic conductivity. The isotherms are composed of three regimes showing universal features in conductivity spectroscopy, see text for further explanation. (b) Change of M''/ω as a function of inverse temperature, measured for the two frequencies indicated (fresh sample, pellet 2). The peaks obtained give rise to two different activation energies characterizing ion dynamics in $LiBH_4$-LiI/Al_2O_3. The high-T flank corresponds to long-range ion dynamics (0.39 eV), whereas the low-T flank (0.23 eV) points to electrical relaxation processes proceeding on a shorter length scale. M''/ω peaks were recorded at 1.15 MHz and 10 MHz, respectively. The kink marked by the dashed arrow indicates that low-dimensional features are masked by the fact that, at sufficiently high temperature, the quantity M''/ω is governed by DC conductivity values rather than by the dispersive regimes of the conductivity isotherms; see text for further details.

senses the presence of Al_2O_3 causing this extra line in NMR spectroscopy.

Finally, we used ^{27}Al NMR spectroscopy to visualize any unsaturated Al centers near or at the surface regions of the alumina scaffold, see Figure 1d. Indeed, pure Al_2O_3, which is here present in its γ-modification, produces a ^{27}Al MAS NMR spectrum that is not only composed of the signals reflecting six- and four-fold-coordinated Al species, see the signals at 9 ppm and at ca. 65 ppm, but is also including a line at approximately 30 ppm (Figure 1d). Although the intensity of the line is low, we are certain that it represents unsaturated pentacoordinated Al ions near the surface of the oxide.[50,52] The generation of such pentacoordinated sites has been studied for nanocrystalline γ-Al_2O_3,[52] which can be prepared by high-energy ball-milling. These sites can be saturated if foreign anions, such as F^- anions from CaF_2 or LiF, are offered.[36,52] As a consequence, the signal disappears since $[AlO_5F]$ will give rise to NMR lines with chemical shifts highly comparable to that of $[AlO_6]$. Indeed, this phenomenon is also seen in the present case, see Figure 1d. For both $LiBH_4$/Al_2O_3 and $LiBH_4$-LiI/Al_2O_3, we observe only the main signals reflecting $[AlO_6]$ and $[AlO_4]$. This comparison shows that, at least to a certain degree, the anions I^- and BH_4^- interact with the $[AlO_5]$ surface groups, which serve as anchoring points for these anions. In nanocomposites of LiF/Al_2O_3, this interaction influences Li^+ transport, as Li^+ is assumed to be electrostatically bound to the $[AlO_5F]$ sites.[36] The complex $[AlO_5F]^-$ Li^+ leaves behind Li^+ vacancies being necessary for the other Li^+ ions to perform hopping processes in the vicinity of the surface regions. Such a surface-controlled diffusion mechanism might be a universal feature of conductor/insulator composites with γ-Al_2O_3 equipped with unsaturated species in interfacial

regions. As in the case of LiF/Al_2O_3[36] or LiI/Al_2O_3,[37] percolating surface pathways would give rise to enhanced long-range Li ion transport. Here, also, hydroxyl surface groups might strongly influence Li^+ interfacial ionic transport as has been suggested by us recently.[11]

Importantly, the asymmetry of the NMR signal belonging to $[AlO_6]$ (and $[AlO_4]$) showing a tail in the direction of low chemical shift values serves as a classical indication of disordering. As $LiBH_4$-LiI (and $LiBH_4$ without LiI) infiltrates the pores of the oxide support, we attribute disordering to the generation of strain and polyhedra distortions experienced by the Al species on or near the surface of the oxide. ^{27}Al multiquantum MAS NMR might be helpful to characterize this effect in future studies.

3.2. Impedance Spectroscopy and Resistivity Measurements at Fixed Frequency. Figure 2a includes selected conductivity isotherms of $LiBH_4$-LiI/Al_2O_3, which show the real part, σ', of the complex conductivity as a function of frequency ν. The isotherms are composed of three regimes. Regime I is caused by polarization effects appearing at sufficiently low frequencies and high DC conductivity values. DC conductivities σ_{DC} can be read off from the frequency-independent plateaus spanning, at $\vartheta = 20$ °C, a frequency range of six orders of magnitude (regime II). At this temperature, the ionic bulk conductivity σ_{DC} is in the order of 0.1 mS cm^{-1}, see the horizontal arrow in Figure 2a. With increasing frequency, the DC plateau passes into regime III, which is the dispersive region being characteristic for correlated, forward-backward jump processes and electrical relaxation processes proceeding on a shorter length scale. This regime is best seen at low temperatures and high frequencies, see Figure 2a.
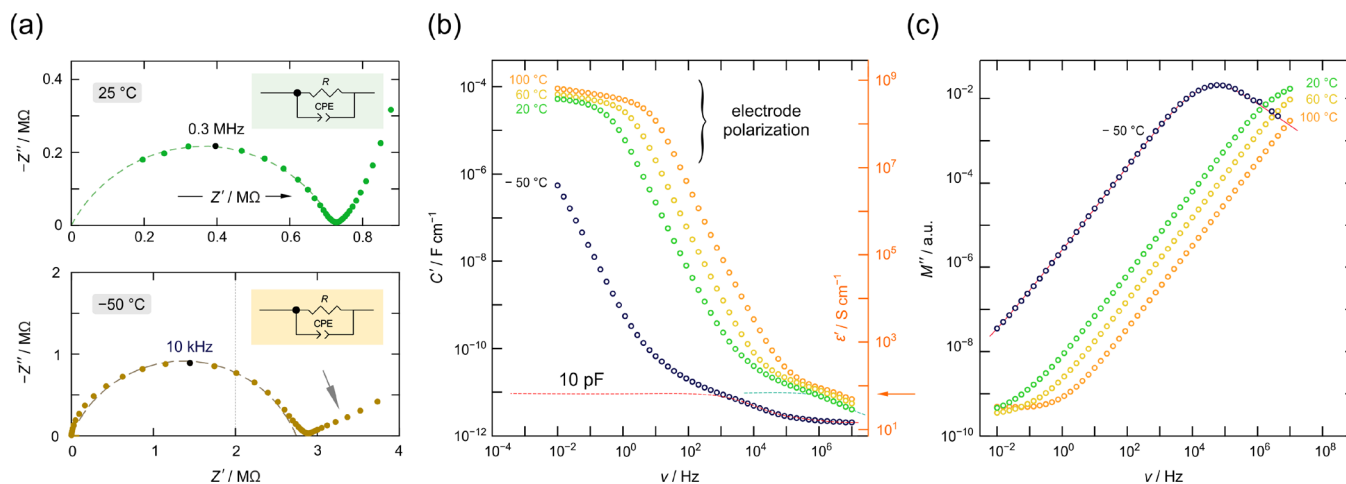
Figure 3. (a) Nyquist plots showing the electrical response of nanoconfined LiBH$_4$-LiI/Al$_2$O$_3$ as the location curve of $-Z''$ as a function of Z' at two different temperatures, viz., recorded at 25 °C and −50 °C. The dashed lines show simulations of the semicircle with the equivalent circuit shown. The response at low frequencies reflects electrode polarization, see also (b). In contrast to the spike seen at 25 °C, the flat response of the location curve referring to −50 °C (see arrow) might indicate the influence of interfacial electrical relaxation processes. (b) Real part of the capacitance as a function of frequency. The curves correspond to the conductivity isotherms shown in Figure 2a; the right axis shows the change of ε' with frequency. (c) Modulus spectra of nanoconfined LiBH$_4$-LiI/Al$_2$O$_3$ recorded at the temperatures indicated.
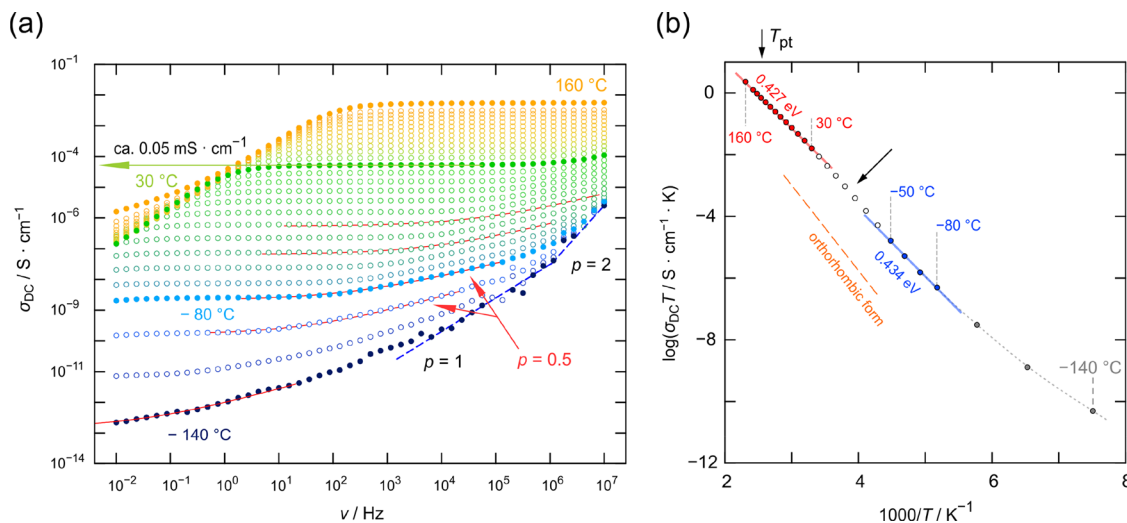

Figure 4. (a) Full set of conductivity isotherms recorded at temperatures ranging from −140 to 160 °C. The solid lines show power law fits revealing that the dispersive regime directly associated with the DC response has to be characterized by an exponent $p = 0.5$, which points to 2D ionic conduction. The DC response corresponds to the conductivities in the limit $\nu \rightarrow 0$ excluding polarization effects. At lower temperatures, the frequency dependence in the dispersive regime changes from $p = 1/2$ to $p = 1$ and further to $p = 2$. While $p = 1$ is consistent of nearly constant loss behavior of the imaginary part of the complex permittivity, $p = 2$ indicates the influences of phonons on σ'. (b) Change of the DC conductivity with temperature, plotted as $\log_{10}(\sigma_{DC}T)$ vs $1000/T$. The position $\sigma_{DC}T$ of microcrystalline LiBH$_4$ (orthorhombic modification) is also shown;[29] data reproduced with permission from ref 29. Copyright 2010 John Wiley and Sons.

The DC plateau together with its dispersive regime produces a single depressed, i.e., non Debye, semicircle in the complex plane plot; two of these plots are exemplarily shown in Figure 3a. They show the imaginary part, $-Z''$, of the complex impedance as a function of the real part, Z'. Simulating the main electrical response with an equivalent circuit consisting of a resistor connected in parallel with a constant phase element, as shown in the inset of Figure 3a, yields a capacity of 6.5 pF, which lies in the expected range for values of bulk processes. Values in the order of 10 pF are also estimated for this electrical process if we take a look at the change of the real part of the complex capacitance C' as a function of frequency, see the first step of the $C'(\nu)$ when coming from high frequencies, which is marked by the dashed lines drawn. In terms of ε',

which is the real part of the complex permittivity, this values corresponds to $\varepsilon'(\nu \rightarrow 0) \approx 80$, see the right axis of Figure 3b. The shape of the corresponding complex modulus $M''(\nu)$ is shown in Figure 3c. At $\vartheta = -50$ °C, the characteristic relaxation frequency reaches values in the order of 10^5 Hz. In all three plots (Figure 3a−c), neglecting the effect of polarization of the ion blocking electrodes, a single electrical response characterizes the overall behavior. Hence, from the point of view of electrical relaxation, nanoconfined LiBH$_4$-LiI/Al$_2$O$_3$ behaves like a homogenous matrix. Considering the small pore size of 9 nm, see above, this result seems to be quite reasonable as the inner regions of the pores are expected to be affected by space charge or surface effects. Here, we cannot see distinct responses that exclusively reflect relaxation in or near
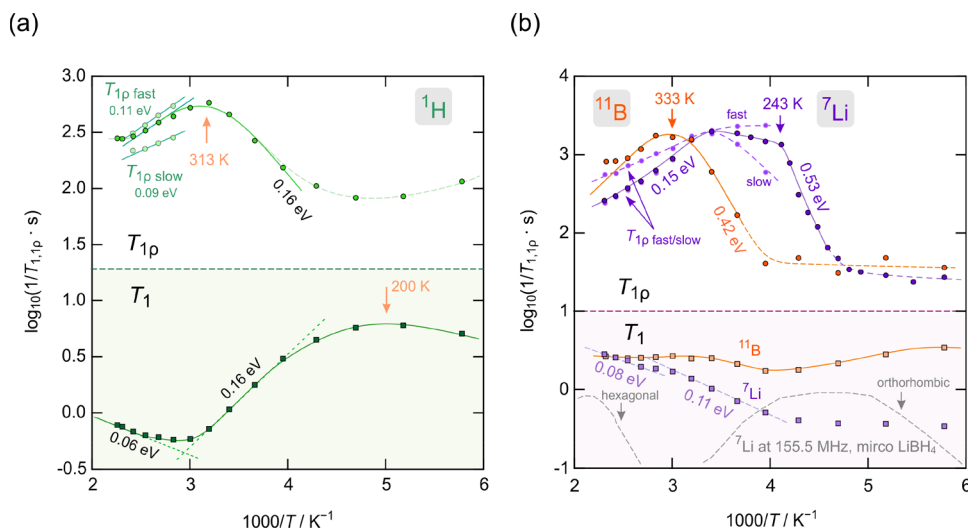
Figure 5. (a) Arrhenius plot revealing the temperature behavior of the ^{1}H NMR spin−lattice relaxation rates $1/T_1$ of LiBH$_4$-LiI/Al$_2$O$_3$ (lower graph). The corresponding rates $1/T_{1\rho}$ recorded in the rotating frame of the reference 20 kHz locking frequency are also shown, see the upper graph. Above 330 K, a separation of two rates according to their distinct T_2 spin−spin relaxation times is possible. (b) ^{7}Li and ^{11}B NMR spin−lattice relaxation rates as a function of the inverse temperature. Spin-lock NMR rates (20 kHz) are shown in the upper part of the Figure; again, a separation into two sub-ensembles is possible indicated by the rates $1/T_{1\rho,slow}$ and $1/T_{1\rho,fast}$. Dashed and dotted lines are drawn to guide the eye. Values show activation energies calculated from the slopes of the lines drawn. The behavior of $1/T_1$ of ^{7}Li of coarse-grained (microcrystalline) LiBH$_4$ is indicated by dashed lines (155 MHz), data reproduced with permission from ref 29. Copyright 2010 John Wiley and Sons.

interfacial regions and regions farther away from the surface. This observation is in agreement with the ^{6}Li MAS NMR and, partly, also with the ^{7}Li NMR line shapes, see below. These lines, because of sufficiently rapid Li$^+$ exchange, do not point to strongly dynamically distinct Li ions. This dynamic homogeneity seen does also agree with the shape of the resistivity peaks recorded, see Figure 2b.

In Figure 2b, the change of the resistivity expressed as M'' divided by frequency ω is shown. M'' is the imaginary part of the electrical modulus. $\rho'_M = M''/\omega$ is given by $\rho'_M = \tau_\rho/(1 + (\tau_\rho\omega)^\beta)$ with $1 < \beta \leq 2$ where τ_ρ denotes the electrical relaxation time, and β is a parameter that quantifies the deviation of the Lorentzian-shaped peak $\log_{10}(\rho'_M)$ versus $1/T$ from symmetric behavior. For $\beta = 2$, symmetric rate peaks would be obtained. $E_{a,high} = 0.39$ eV and $E_{a,low} = 0.23$ eV are related to each other via $E_{a,low} = (\beta - 1)E_{a,high}$ yielding $\beta \approx 1.6$. This view on ρ'_M is comparable to that of NMR spin−lattice relaxation measurements, see below. The shape of the $\rho'_M(1/T)$ peak, which points to length-scale-dependent heterogeneous electrical relaxation, agrees with the observation of a depressed, non Debye semicircle in the complex plot $-Z''(Z')$ as well as with the dispersive signature of the conductivity isotherms $\sigma'(\nu)$, which is seen at sufficiently low temperatures (regime III in Figure 2a).

Importantly, we notice that the shape of the ρ'_M peaks near the maximum is composed of two contributions. The arrow in Figure 2b marks a kink (380 K) most likely showing the crossover from ρ'_M values being influenced by regime III and those governed by regime II. The latter influence is seen at higher temperatures where $\rho'_M(1/T)$ follows an Arrhenius behavior with $E_a = 0.39$ eV. This activation energy agrees well with that of $\sigma_{DC}T(1/T)$, see Figure 4b, characterizing long-range ion transport. ρ'_M values recorded below 380 K, see the curve measured at 10 MHz, reveal a frequency-dependent behavior if we compare the resistivity values measured at 10 Hz with those recorded at 1.2 MHz, cf. the dashed lines drawn.

Such a dispersive behavior is here interpreted as a result of 2D ionic conduction in the interior regions of LiBH$_4$-LiI/Al$_2$O$_3$.

The frequency dependence of the conductivity isotherms in regime III of Figure 2a supports this idea. They are composed of a dispersive regime that also points to low-dimensional ionic transport in LiBH$_4$-LiI/Al$_2$O$_3$. In general, for hexagonal LiBH$_4$, being stable at temperatures above 110 °C, 2D Li$^+$ self-diffusion was proved by frequency-dependent ^{7}Li and ^{6}Li NMR relaxation.[57] If the hexagonal modification is, however, stabilized at sufficiently low temperatures, the dispersive regime of the $\sigma'(\nu)$ becomes detectable, which should contain information about dimensionality effects. In Figure 4a, a full set of conductivity isotherms recorded over a much larger temperature range than that covered by Figure 2a is shown. For these variable-temperature σ' measurements, we used a second, fresh pellet to probe regime III in detail. Although σ_{DC} is somewhat lower for this pellet (0.05 mS cm^{-1} at 20 °C), the dispersive part is perfectly seen over a large frequency range. If it is approximated with Jonscher's power law[58] $\sigma'(\nu) \propto \nu^p$, we obtain $p = 0.5$. It has been shown earlier that an exponent p of 1/2 is a valid argument pointing to 2D ionic conduction.[59] For 3D ion transport, p is expected to take values of 0.6−0.9, while 1D (channel-like) transport should result in $p < 0.4$.[59]

Here, the idea of 2D ionic transport restricts to the LiBH$_4$-LiI regions of the sample. As mentioned above, at higher T, the resistivity values are mainly governed by σ_{DC} rather than by $\sigma'(\nu) \propto \nu^p$. Hence, we conclude that effectively 3D ionic conduction is established on a long-range length scale in LiBH$_4$-LiI/Al$_2$O$_3$, while 2D ion transport is seen on a shorter-length scale.

To further analyze long-range ionic transport, we read off σ_{DC} values from the isotherms presented in Figure 4a. In Figure 4b, the change of $\sigma_{DC}T$ with $1/T$ for pellet 2 is shown. In above ambient conditions, we see that the data points follow Arrhenius behavior with an activation energy of $E_a = 0.427$ eV. At approximately $\vartheta = -50$ °C, a slight curvature appears (see arrow) slightly reducing the ionic conductivity while almost
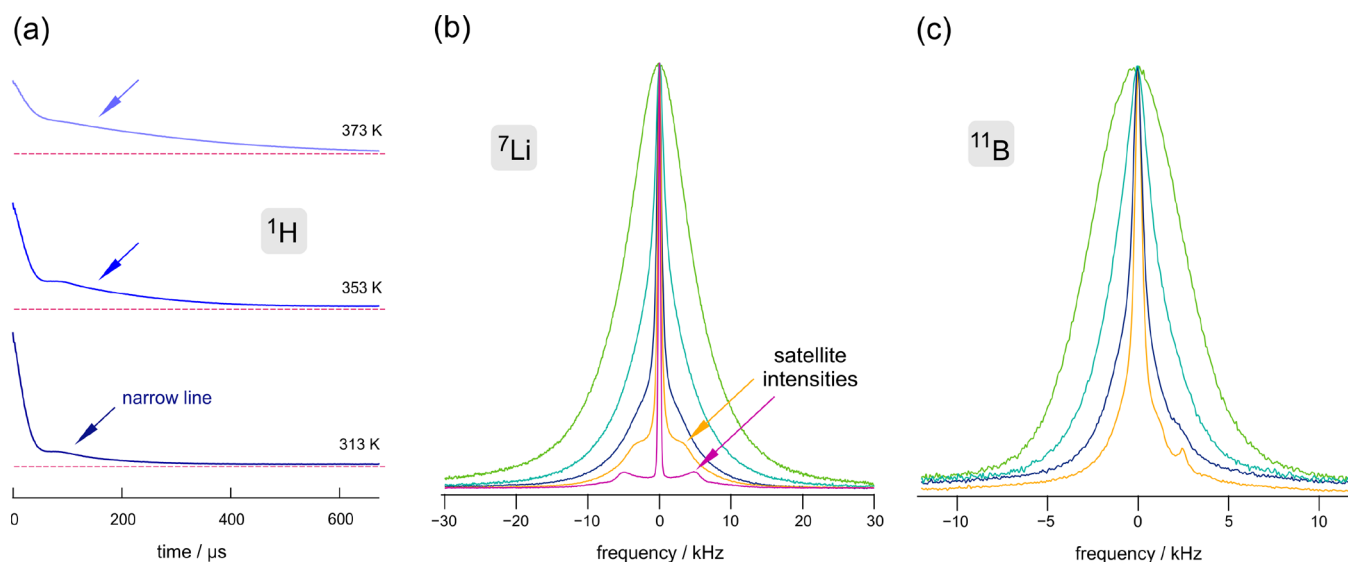
Figure 6. (a) ^1H NMR FIDs (300 MHz) of LiBH$_4$-LiI/Al$_2$O$_3$ measured at the temperatures indicated. The FIDS are composed of two contributions reflecting two ^1H sub-ensembles that differ in spin−spin relaxation behavior. (b, c) Variable-temperature ^7Li (116 MHz) and ^{11}B NMR (96 MHz) spectra (173, 253, 294, 313, and 433 K) of nanoconfined LiBH$_4$-LiI/Al$_2$O$_3$. In the case of ^7Li NMR, distinct satellite intensities show up at high temperatures.

unchanging the activation energy. Thus, this change is mainly caused by a slight reduction of the pre-exponential factor σ_0 in $\sigma_{DC}T = \sigma_0 \exp(-E_a/(k_BT))$ where k_B denotes Boltzmann's constant. The prefactor contains, among other quantities, the effective number of charge carriers, the attempt frequency, and an activation entropy term; thus, a range of factors can cause this slight difference. Below −100 °C, the values seem to be influenced by further conduction processes because $\sigma_{DC}T$ turned out to be higher than expected if the Arrhenius line, which is characterized by $E_a = 0.434$ eV, is extrapolated toward lower T, see Figure 4b. Likely, electronic conduction might influence the overall DC conductivity of such a nanostructured sample in this low-T range. Most importantly, even up to temperatures well below ambient, we do not find strong indications that the material transforms from its hexagonal modification, stabilized by the incorporation of LiI, to the orthorhombic form. The latter, if present in a coarse-grained form or being in contact with Al$_2$O$_3$ in the sense of a dispersed ionic conductor, shows a much lower ionic conductivity.[29] For comparison, the ionic conductivity of microcrystalline orthorhombic LiBH$_4$ with a crystallite diameter in the micrometer (μm) range is indicated by a dashed line in Figure 4b. The original temperature T_{pt} at which the phase transition occurs (ca. 110 °C) is also indicated, see the arrow pointing at the upper axis. In conclusion, we do not find any evidence for a marked phase transition for LiBH$_4$-LiI/Al$_2$O$_3$. Quite the contrary, we assume that nanoconfinement supports the stabilization of the hexagonal phase of LiBH$_4$-LiI nanoconfined in alumina. 2D ionic conduction seems to be the prevailing transport mechanism in LiBH$_4$-LiI as revealed by the $p^{0.5}$ frequency behavior seen in $\sigma'(\nu)$ measurements, as has also been suggested by other methods and theory.[57,60−62]

3.3. ^1H, ^7Li, and ^{11}B NMR Spin−Lattice Relaxation in LiBH$_4$-LiI/Al$_2$O$_3$.

In Figure 5, the temperature behaviors of the NMR spin−lattice relaxation rates ^1H, ^{11}B, and ^7Li of LiBH$_4$-LiI/Al$_2$O$_3$ are shown. As nuclear spin relaxation is sensitive to both long-range and short-range ion dynamics, including translational processes, rotational motions, and even librations, we expect a wide range of activation energies probed by NMR.

Indeed, the diffusion-induced rates, if analyzed in the frame of Arrhenius representations, yield a couple of different flanks pointing to activation energies ranging from 0.06 to 0.53 eV. A similar situation has been met for cation-disordered fluorides.[63]

3.3.1. ^1H NMR Spin−Lattice Relaxation. Starting with ^1H NMR, see Figure 5a, we see that, below 300 K, the laboratory-frame $1/T_1$ rates pass through a broad maximum. Most likely, this peak reflects rotational BH$_4^-$ motions as a very similar behavior has been documented for LiBH$_4$. The slight increase in $1/T_1$ above 300 K is attributed to either H-dynamics or localized Li$^+$ motions indirectly sensed by the ^1H probes or H-dynamics. The associated apparent activation energy of 0.06 eV points to correlated ionic motion proceeding on a local length scale. At even higher temperatures, one would expect the rate to pass through a diffusion-induced maximum. With decreasing Larmor frequency, this maximum would be shifted toward lower T. The corresponding peak $1/T_1(1/T)$ should occur at T_{max} where the motional correlation rate $1/\tau_c$ reaches the angular Larmor frequency ω_0 ($= \nu_0 \times 2\pi = 300$ MHz $\times 2\pi$) fulfilling the relationship $\tau_c\omega_0 \approx 1$. $1/\tau_c$ is within a factor of 2 identical with the Li$^+$ jump rate,[64] provided the peak is solely caused by Li$^+$-translational jumps. Replacing ω_0, having values in the megahertz (MHz) range, by ω_1, being the spin-lock frequency in the kilohertz (kHz) range, will shift this peak considerably toward lower T.[64] As can be seen in the upper graph of Figure 5a, such a peak indeed appears at $T_{max} = 313$ K. This peak corresponds to a similar diffusion-induced peak seen in ^{11}B NMR (333 K, Figure 5b), see below. The activation energy of the ^1H NMR peak probed by $1/T_{1\rho}$ is 0.16 eV. This value agrees with that from the M''/ω analysis if we consider the low-T flank of the $\rho'_M(1/T)$ peak (0.21 eV, 100 kHz, see Figure 2b). We also observed that $1/T_{1\rho}$ of ^1H increases at temperatures lower than 200 K. At such low temperatures, the rate $1/T_{1\rho}$ is expected to pass through another rate peak, which corresponds to the behavior of $1/T_1$ ($T_{max} = 200$ K), presumably characterizing fast rotational BH$_4^-$ dynamics.

Noteworthy, the ^1H (spin-1/2) NMR rates shown in Figure 5a were extracted from magnetization transients that were constructed by analyzing the full area under the corresponding
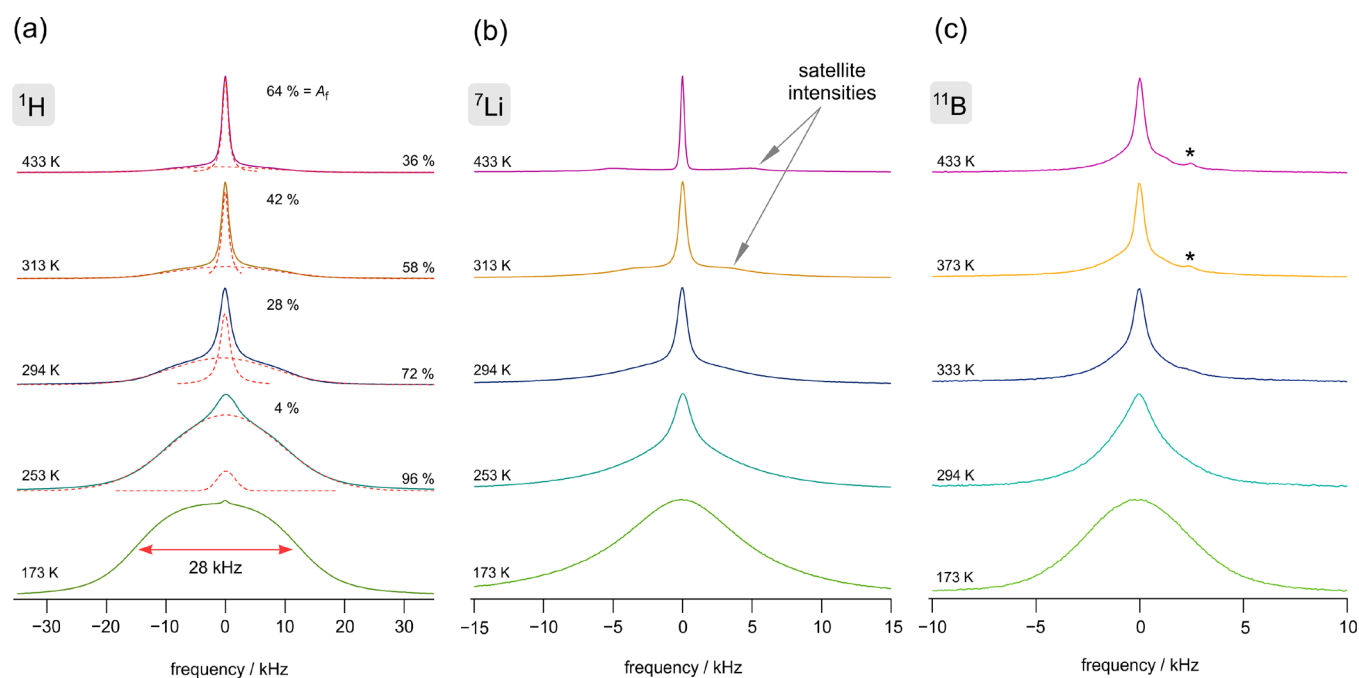
Figure 7. (a) ^1H NMR spectra of $LiBH_4$-LiI/Al_2O_3 being composed of two spectral components reflecting two dynamically distinct ^1H spin ensembles. Dashed lines show deconvolutions of the spectra with Gaussian and Lorentzian functions. (b, c) ^7Li and ^{11}B spectra as in Figure 6 but shown in a stacked plot to highlight the Gaussian shape of the lines at low temperatures.

FIDs, see Figure 6a. The resulting transients show stretched exponential behavior, see Experimental Section. However, as can be seen in Figure 6a, we observed so-called two-component FIDs at temperatures above ambient. Such a two-component FID is composed of a slowly decaying part, which can be well separated from a fast-decaying contribution dominating the FID at short acquisition times. Consequently, Fourier transformation leads to ^1H NMR spectra showing two contributions, as presented in Figure 7a.

The motionally narrowed contribution represents ^1H spins sensing magnetic-dipolar fluctuations being fast on the NMR spectral time scale, i.e., the corresponding motional correlation greatly rate exceeds the rigid lattice line width (28 kHz at 173 K, see Figure 7a). With increasing temperature, the majority of the ^1H spins benefit from this motional averaging process resulting in an overall line shape, which is mainly dominated by the narrow line. The change in area fraction A_f of this line, on top of the broad one, is indicated in Figure 6a; A_f reaches values as high as 64% at 433 K. At room temperature, approximately one third of the ^1H spins participate in a rather fast dynamic process. In general, one would assign the narrow line to those H spins located in the interfacial regions. On the other hand, the two-component line shape could also originate from strongly heterogeneous dynamics of the whole spin ensemble, see below.

To test whether these two spectral contributions with individual spin−spin relaxation times are also characterized by distinct $1/T_1$ rates, we analyzed parts of the underlying FIDs in the frame of a saturation recovery experiment. This procedure has been explained in detail elsewhere.[65] Here, no difference in $1/T_1$ is observed between the rates obtained either by analyzing the full FID or the two differently decaying parts highlighted in Figure 7a. This finding points to fast-spin diffusion connecting the two ^1H spin reservoirs with their distinct spin−spin relaxation behavior. Spin diffusion due to fast flip−flop processes results in a single, averaged spin−lattice

relaxation behavior. It is, however, in contrast for ^1H spin-lock $1/T_{1\rho}$. The circles in light green in Figure 5a show that it is possible to obtain two rates, which we call $1/T_{1\rho,fast}$ (0.11 eV) and $1/T_{1\rho,slow}$ (0.06 eV). The rates differ by a factor of 2 to 3, at most. Importantly, they follow nearly the same temperature behavior (0.09 eV) as seen for the mean rates $1/T_1$ in this T range. Thus, spin-diffusion seems to be present too; however, it turns out to be less effective as in the case of ^1H NMR spin−lattice relaxation characterized by the rate $1/T_1$.

3.3.2. ^7Li and ^{11}B NMR Spin−Lattice Relaxation. The ^7Li and ^{11}B NMR spin−lattice relaxation NMR rates $1/T_1$ and $1/T_{1\rho}$ are shown in Figure 5b, the evolution of the corresponding spectra with temperature is again presented in Figures 6 and 7. In contrast to ^1H, the ^7Li $1/T_1$ NMR rates do not reveal a strong influence of BH_4^- rotations at low T. Rather, below 250 K, the rates are influenced by nondiffusive background relaxation. Above this temperature, they pass into a flank with an activation energy characterized by 0.11 eV. A slight curvature is seen at 340 K; above this temperature, E_a reduces to 0.08 eV. As for ^1H, we assign these low values of E_a to short-range dynamics in nanoconfined $LiBH_4$-LiI/Al_2O_3. For comparison, in Figure 5b, the ^7Li NMR rates of coarse-grained $LiBH_4$ are also included.[29,57] While in hexagonal $LiBH_4$, present above $T_{pt} \approx 100$ °C, the rates are induced by Li^+ diffusion; below this temperature, they reflect BH_4^- rotational dynamics. The ^7Li NMR response of $LiBH_4$-LiI/Al_2O_3 turned out to be completely different to that seen for the source material showing that, from a dynamic point of view as seen by NMR, anion substitution and nanoconfinement have turned the ionic conductor into a completely different material.

$1/T_{1\rho}$ of ^7Li reveals a more complex behavior compared to that observed for the corresponding $1/T_1$ rates, Figure 5b. A nondiffusion-induced background appeared below $T = 210$ K. Above this temperature, the rates, however, sharply increase. This increase is characterized by an activation energy of 0.53 eV, which is very similar to the activation energy extracted

from the $\rho'_M(1/T)$ peak in the high-T limit (0.57 eV, Figure 2b). Obviously, spin-lock ^{7}Li NMR, if carried out at a locking frequency of 20 kHz, is able to sense long-range ion dynamics. The above-mentioned curvature seen in $1/T_1$ might correspond to the maximum in $T_{1\rho}$ seen at 243 K. At higher temperature than 243 K (Figure 5b), the behavior of $1/T_{1\rho}(^7$Li$)$ can only be understood if we consider several relaxation rate peaks contributing to the overall response. Interestingly, the flank seen at high T is again characterized by an activation energy (0.15 eV, Figure 5b) that resembles those seen by $1/T_1(^7$Li$)$; it is also comparable to the values obtained from ^{1}H NMR, see above.

Similar to ^{1}H NMR, also, the FIDs of the ^{7}Li nucleus are, at least to some extent, composed of several components if results above $T = 230$ K are regarded (not shown for the sake of brevity). The corresponding spectra are displayed in Figures 6b and 7b. As ^{7}Li is a spin-3/2 nucleus,[66] the sharply decaying part of its FID partly (or mainly) originates from electric quadrupole interactions, which are characteristic for LiBH$_4$, if present in its hexagonal modification. ^{7}Li NMR spectra have been discussed in detail elsewhere;[11] worth noting, at each temperature, the lines are to be characterized by a single, averaged quadrupole powder pattern with distinct 90° singularities appearing at a distance of ±5 kHz from the central line. They result in a quadrupole splitting of $\Delta \approx 10$ kHz (Figures 6b and 7b). Hence, also from the point of view of quadrupolar electric interactions, the Li ions belong a single ensemble with electrically equivalent spins. We do not see the original electrical powder patterns of LiBH$_4$ ($\Delta \approx 18.5$ kHz) or LiBH$_4$-LiI ($\Delta \approx 18.6$ kHz) any longer. In our earlier publication,[11] we speculated that both the ions near the Al$_2$O$_3$ surface regions, possibly influenced by (residual) hydroxyl surface groups,[11] and those farther away are subjected to a structurally stressed LiBH$_4$-LiI phase with high ionic conductivity. Space charge zones,[35,41] high defect densities or increased structural disorder[34] may characterize these inner, interfacially influenced regions leading to a magnetically and electrically homogenous phase showing enhanced, but heterogeneous, ion dynamics.

The other part of the ^{7}Li NMR FIDs, which forms the central NMR line after Fourier transformation, may also represent ^{7}Li sub-ensembles differing in spin−spin-relaxation times. A clear separation as in the case of ^{1}H NMR is, however, fraught with difficulties. Thus, we cannot precisely identify Li$^+$ ions in the interfacial regions undergoing rapid exchange processes as those spins residing farther away from these regions are involved in rapid diffusion also. The same situation was met in Li$_x$TiS$_2$ for which structural disorder did not lead to a significant enhancement of Li$^+$ dynamics. In layer-structured TiS$_2$, the mobility of Li$^+$ is already rather high.[67] Here, as in the case of ^{1}H spin−lattice relaxation $1/T_1$, the different contributions to the ^{7}Li FIDs undergo the same ^{7}Li spin−lattice relaxation recovery. Again, we conclude that they belong to a magnetically homogeneous Li spin ensemble affected by rapid spin diffusion. Such an ensemble is also suggested by the thermally coalesced ^{6}Li MAS NMR signal discussed above.

For comparison, this finding is in contrast for nanocrystalline, poorly conducting orthorhombic LiBH$_4$ presented in literature quite recently.[38] Its ^{7}Li NMR lines show well-defined two-component line shapes and biexponential magnetization transients at different temperatures. Note that in the orthorhombic modification, Li$^+$-translational ion dynamics is much lower than in the hexagonal form. Only in the interfacial regions of nanocrystalline, orthorhombic LiBH$_4$-fast Li$^+$ ions (0.18 eV) were found that could separately be studied by ^{7}Li NMR spin−lattice relaxation.[38] A very similar result has been seen by ^{7}Li NMR in LiI/Al$_2$O$_3$ mixtures investigated by Ardel et al.[37] In such mixtures one Li$^+$ site has been associated with surface or interface regions.

A separation, being similar to that discussed and carried out for ^{1}H NMR, is only partly possible for the ^{7}Li NMR spin-lock rates $1/T_{1\rho}$. While $1/T_{1\rho,slow} = 1/T_1$, the rates $1/T_{1\rho,fast}$ reveal an even weaker temperature dependence than $1/T_1$ (0.11 eV vs 0.15 eV), see Figure 5b. Again, we interpret such low activation energies as a signature for fast, but localized, dynamic processes, which do not necessarily lead to long-range Li$^+$ ion transport. Alternatively, they might reflect fast Li$^+$ dynamic processes near the conductor/insulator interface,[42] as also seen for nanocrystalline orthorhombic LiBH$_4$ (0.18 eV).[38]

The ^{11}B NMR spin−lattice relaxation rates, see Figure 5b, reveal two shallow NMR rate peaks. The one at lower T could again be assigned to rotational ion dynamics, while the exact origin of that seen at higher T remains unknown. In general, it is well known for LiBH$_4$ that the BH$_4^-$ units undergo fast rotational motions. Moreover, also, the presence of translational ion dynamics has been suggested on the basis of ^{11}B NMR.[26,68] Interactions with the alumina scaffold might change this dynamic behavior of the anions. Here, in ^{11}B spin-lock NMR, we observed a single peak located at $T_{max} = 313$ K; it might indeed be caused by a slower Li translational process indirectly seen by the ^{11}B spins or by BH$_4^-$ translational motions, which were suggested for LiBH$_4$.[27] Interestingly, the activation energy extracted from the ^{11}B $1/T_{1\rho}(1/T)$ NMR is very similar to that seen by $\sigma_{DC}T$; hence, this agreement supports the idea that, at least from a quantitative point of view, the peak is influenced by Li$^+$-hopping processes.^{11}B NMR spectra (spin-3/2) are shown in Figures 6c and 7c. A tiny line, which is marked by an asterisk in Figure 7c, points to a side phase that has already been discussed for ^{1}H MAS NMR, see above. ^{11}B NMR spectra are mainly governed by central lines that are flanked, at least at high temperatures, by satellite intensities. Alternatively, the broad spectral component could be interpreted as a signal arising from less mobile BH$_4^-$ units.

3.4. Long-Range Ion Transport and Diffusion Coefficients as Probed by NMR and Electrical Measurements.

NMR spin−lattice relaxation measurements reveal a rather complex picture of the magnetic fluctuations taking place in nanoconfined LiBH$_4$-LiI/Al$_2$O$_3$. Apart from rapid localized ion dynamics, a practical parameter being relevant for battery applications is the macroscopic (self-)diffusion coefficient D of the Li ions. Here, we took advantage of ^{7}Li PFG NMR measurements to probe tracer diffusion coefficients D_{PFG} at two different temperatures, see the Arrhenius plot of Figure 8.

To compare the results from PFG NMR with those from conductivity spectroscopy, we used the Nernst−Einstein equation, $D_\sigma = (\sigma_{DC}k_BT)/(Nq^2)$, to convert σ_{DC} into solid-state diffusion coefficients; in Figure 8, the results for the two pellets are included. Here, N is the charge carrier density, which we estimated to be approximately 1.8×10^{27} m^{-3}, q denotes the charge of the Li$^+$ ions. Here, we simply used the chemical formula of LiBH$_4$-LiI/Al$_2$O$_3$ and assumed that all Li$^+$ ions participate in diffusion. The effective number might be lower and should be related to the exact defect structure of the
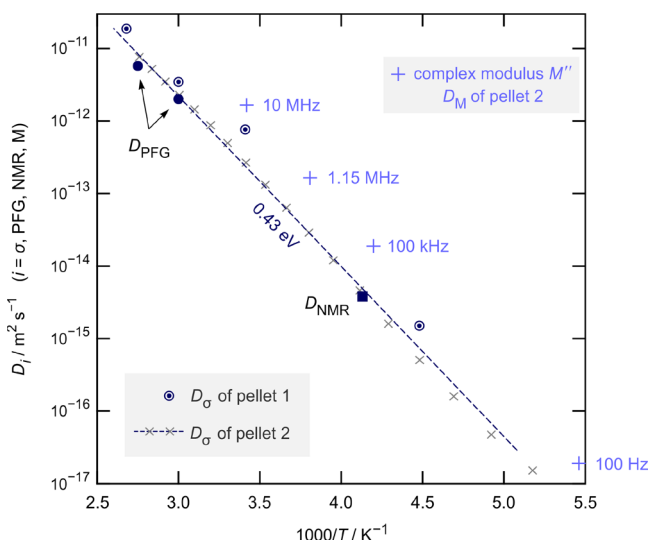
Figure 8. Arrhenius plot illustrating the temperature dependence of the diffusion coefficients D_i ($i = \sigma$, PFG, NMR, M) deduced from the various methods applied to study long-range ion dynamics in nanoconfined LiBH$_4$-LiI/Al$_2$O$_3$. Depending on temperature, the difference between D_σ values of pellets 1 and 2 turned out to be a factor of 3 (at most). The dashed line is a guide to the eye whose slope corresponds to an activation energy of 0.43 eV. Coefficients deduced from electric modulus spectroscopy (pellet 2) are also included. They run in parallel but are shifted toward larger values. Such a discrepancy can be described to length-scale-dependent dynamics. While σ_{DC} senses long-range ion dynamics, electric modulus data might already be influenced by short-range ion dynamics.

material. Moreover, this estimate holds only under the assumption of Li$^+$ being the sole charge carrier.

In addition, to estimate D_{NMR}, we used the result from ^{7}Li NMR spin-lock measurements. As mentioned above, the relation $\omega_1\tau_c \approx 1$ holds for spin-lock relaxation $1/T_{1\rho}$. To estimate $D_{NMR} = a^2/(4\tau_c)$ we used the ^{7}Li NMR peak $1/T_{1\rho}$ that appears at $T_{max} = 243$ K, see Figure 5b. a (= 4.26 Å) is the nearest-neighbor distance of a Li$^+$ ion in the hexagonal lattice. Finally, we estimated diffusion coefficients D_M from the M''/ω peak maxima by assuming that at T_{max} the associated electrical relaxation time is given by $\omega\tau_e \approx 1$ with ω being the fixed measurement frequency. D_M was calculated by means of the Einstein–Smoluchowski equation,[34] which reads for 2D diffusion $D_M = a^2/(4\tau_M)$.

In general, differences between D_{PFG} and D_σ can be explained by the Haven ratio H_r deviating from $H_r = 1$. If we identify D_{PFG} with the tracer diffusion coefficient D_{tracer}, the two diffusion coefficients are related to each other via $D_{tracer} = H_r D_\sigma$. On the other hand, D_{NMR} and D_{tracer} are linked via the correlation factor f ($0 < f \leq 1$): $D_{tracer} = f D_{NMR}$. Altogether, this leads to $D_{NMR} = (H_r/f)D_\sigma$. Hence, the factor H_r/f deviating from 1 can explain the rather small differences between the coefficients shown in Figure 8. Despite these differences, the results for D_σ, D_{PFG}, and D_{NMR} shown in Figure 8 agree well with each other. As indicated by the straight line, which is used as a guide to the eye here, the data points follow an Arrhenius law with an activation energy of 0.43 eV; at ambient temperature, we estimated the mean diffusion coefficient to be in the order of ca. 3×10^{-13} m^2 s^{-1} (298 K, pellet 2). The shift of D_M toward larger coefficients might be explained by short-range ion dynamics already influencing the maxima of

the resistivity peaks recorded. Indeed, as has been shown by both ^{1}H, ^{7}Li, and ^{11}B NMR line shapes and NMR spin–lattice relaxation measurements quite complex, translational and rotational (and librational) dynamic processes are present including (strictly) localized events determined by much lower activation energies of only 0.06 eV.

4. SUMMARY AND CONCLUSIONS

Overall, long-range ionic transport in nanoconfined LiBH$_4$-LiI/Al$_2$O$_3$ as probed by conductivity spectroscopy follows Arrhenius behavior (0.43 eV) over a dynamic range of almost 8 orders of magnitude. Solid-state diffusion coefficients estimated from conductivity values and variable-temperature resistivity data recorded at fixed frequency agree very well with those obtained from macroscopic ^{7}Li PFG NMR. At room temperature, a diffusion coefficient of 3×10^{-13} m^2 s^{-1} was obtained. ^{1}H, ^{7}Li, and ^{11}B NMR relaxation measurements revealed highly complex dynamics with a broad range of activation energies ranging from 0.06 to 0.57 eV.

Interfacial effects are seen by ^{27}Al MAS NMR; most likely, pentacoordinated sites of the Al$_2$O$_3$ scaffold become saturated through the formation of Li$^+$[AlO$_5$I]$^-$ or Li$^+$[AlO$_5$BH$_4$]$^-$ species; the participation of surface hydroxyl groups has to be considered also, as suggested recently.[11] This view is supported by ^{6}Li MAS and ^{11}B MAS NMR, the latter reveals two B sites slightly differing in the magnetic environment. At least for ^{1}H, the corresponding variable-temperature, two-component NMR line shapes showed H spins subjected to quite different spin–spin fluctuations. Most likely, they reflect spins near interfacial regions and spins farther away from the surface, that is, located in the LiBH$_4$-LiI matrix. As shown by ^{7}Li NMR line shapes and broadband conductivity spectroscopy, the Li spins participate in heterogeneous ion dynamics but; most likely, they belong to an electrically homogeneous ensemble. We speculate that interfacial effects also influence the inner regions of the nanometer-sized pores that are filled with LiBH$_4$-Li. This situation is usually met for nanostructured ion conductors dominated by space charge effects, which are termed artificial ion conductors.[69,70] Specifically, the reaction with hydroxyl surface groups might play a crucial role too since insights into ^{27}Al MAS NMR underpin this assumption.[11]

Finally, the dispersive regions in conductivity spectra follows Jonscher's power law with an exponent of $p = 1/2$. This result points to low-dimensional (2D) ionic transport in the layer-structured, hexagonal LiBH$_4$-LiI regions. We were able to follow this 2D ion transport process down to temperatures as low as −80 °C. On the other hand, NMR and electric modulus spectroscopy carried out at sufficiently high temperatures reveal long-range 3D ion transport, likely involving fast ion conduction also along the interfacial conductor/insulator regions. While for many highly conducting layer-structured materials, grain boundaries may act as regions blocking ion transport; in the case of nanoconfined LiBH$_4$-LiI/Al$_2$O$_3$, such limitations can be overcome by fast-conducting interfacial conductor/insulator regions.

■ ASSOCIATED CONTENT

Ⓢ Supporting Information

The Supporting Information is available free of charge at https://pubs.acs.org/doi/10.1021/acsami.0c10361.

NMR parameters; ^{1}H, ^{7}Li, and ^{11}B NMR relaxation transients; and PFG NMR decay curves (PDF)

■ AUTHOR INFORMATION

Corresponding Authors

Roman Zettl − *Institute for Chemistry and Technology of Materials, and Christian Doppler Laboratory for Lithium Batteries, Graz University of Technology, Graz 8010, Austria; Inorganic Chemistry and Catalysis, Debye Institute for Nanomaterials Science, Utrecht University, Utrecht 3584, Netherlands;* Email: zettl@tugraz.at

H. Martin R. Wilkening − *Institute for Chemistry and Technology of Materials, and Christian Doppler Laboratory for Lithium Batteries, Graz University of Technology, Graz 8010, Austria; Alistore−ERI European Research Institute, CNRS FR3104, Hub de l'Energie, F-80039 Amiens, France;* orcid.org/0000-0001-9706-4892; Email: wilkening@tugraz.at

Authors

Maria Gombotz − *Institute for Chemistry and Technology of Materials, and Christian Doppler Laboratory for Lithium Batteries, Graz University of Technology, Graz 8010, Austria*

David Clarkson − *Department of Physics and Astronomy, Hunter College of the City University of New York, New York 10065 New York, United States*

Steven G. Greenbaum − *Department of Physics and Astronomy, Hunter College of the City University of New York, New York 10065 New York, United States;* orcid.org/0000-0001-5497-5274

Peter Ngene − *Inorganic Chemistry and Catalysis, Debye Institute for Nanomaterials Science, Utrecht University, Utrecht 3584, Netherlands;* orcid.org/0000-0003-3691-0623

Petra E. de Jongh − *Inorganic Chemistry and Catalysis, Debye Institute for Nanomaterials Science, Utrecht University, Utrecht 3584, Netherlands;* orcid.org/0000-0002-2216-2620

Complete contact information is available at:
https://pubs.acs.org/10.1021/acsami.0c10361

Notes
The authors declare no competing financial interest.

■ REFERENCES

(1) Larcher, D.; Tarascon, J.-M. Towards Greener and More Sustainable Batteries for Electrical Energy Storage. *Nat. Chem.* **2015**, *7*, 19−29.

(2) Whittingham, M. S. Inorganic Nanomaterials for Batteries. *Dalton Trans.* **2008**, 5424−5431.

(3) Goodenough, J. B. Evolution of Strategies for Modern Rechargeable Batteries. *Acc. Chem. Res.* **2013**, *46*, 1053−1061.

(4) Zhou, W.; Li, Y.; Xin, S.; Goodenough, J. B. Rechargeable Sodium All-Solid-State Battery. *ACS Cent. Sci.* **2017**, *3*, 52−57.

(5) Pan, H.; Hu, Y.-S.; Chen, L. Room-Temperature Stationary Sodium-Ion Batteries for Large-Scale Electric Energy Storage. *Energy Environ. Sci.* **2013**, *6*, 2338−2360.

(6) Goodenough, J. B.; Kim, Y. Challenges for Rechargeable Li Batteries. *Chem. Mater.* **2010**, *22*, 587−603.

(7) Zhang, Z.; Shao, Y.; Lotsch, B.; Hu, Y.-S.; Li, H.; Janek, J.; Nazar, L. F.; Nan, C.-W.; Maier, J.; Armand, M.; Chen, L. New Horizons for Inorganic Solid State Ion Conductors. *Energy Environ. Sci.* **2018**, *11*, 1945−1976.

(8) Uitz, M.; Epp, V.; Bottke, P.; Wilkening, M. Ion Dynamics in Solid Electrolytes for Lithium Batteries. *J. Electroceram.* **2017**, *38*, 142−156.

(9) Bachman, J. C.; Muy, S.; Grimaud, A.; Chang, H.-H.; Pour, N.; Lux, S. F.; Paschos, O.; Maglia, F.; Lupart, S.; Lamp, P.; Giordano, L.; Shao-Horn, Y. Inorganic Solid-State Electrolytes for Lithium Batteries: Mechanisms and Properties Governing Ion Conduction. *Chem. Rev.* **2016**, *116*, 140−162.

(10) Thangadurai, V.; Narayanan, S.; Pinzaru, D. Garnet-Type Solid-State Fast Li Ion Conductors for Li Batteries: Critical Review. *Chem. Soc. Rev.* **2014**, *43*, 4714−4727.

(11) Zettl, R.; de Kort, L.; Gombotz, M.; Wilkening, H. M. R.; de Jongh, P. E.; Ngene, P. Combined Effects of Anion Substitution and Nanoconfinement on the Ionic Conductivity of Li-Based Complex Hydrides. *J. Phys. Chem. C* **2020**, *124*, 2806−2816.

(12) Jarrett, W. L.; Farlee, R. D.; Butler, L. G. Observation of Bridging and Terminal Metal-Hydrides by Solid-State Deuterium NMR Spectroscopy - Application to Bis(Cyclopentadienyl)Zirconium Dideuteride. *Inorg. Chem.* **1987**, *26*, 1381−1383.

(13) Ravnsbaek, D. B.; Frommen, C.; Reed, D.; Filinchuk, Y.; Sørby, M.; Hauback, B. C.; Jakobsen, H. J.; Book, D.; Besenbacher, F.; Skibsted, J.; Jensen, T. R. Structural Studies of Lithium Zinc Borohydride by Neutron Powder Diffraction, Raman and NMR spectroscopy. *J. Alloys Compd.* **2011**, *509*, S698−S704.

(14) Skripov, A. V.; Soloninin, A. V.; Ley, M. B.; Jensen, T. R.; Filinchuk, Y. Nuclear Magnetic Resonance Studies of BH_4^- Reorientations and Li Diffusion in $LiLa(BH_4)_3Cl$. *J. Phys. Chem. C* **2013**, *117*, 14965−14972.

(15) Züttel, A.; Wenger, P.; Rentsch, S.; Sudan, P.; Mauron, P.; Emmenegger, C. $LiBH_4$ a New Hydrogen Storage Material. *J. Power Sources* **2003**, *118*, 1−7.

(16) Schüth, F.; Bogdanović, B.; Felderhoff, M. Light Metal Hydrides and Complex Hydrides for Hydrogen Storage. *Chem. Commun.* **2004**, *20*, 2249−2258.

(17) Sakintuna, B.; Lamari-Darkrim, F.; Hirscher, M. Metal Hydride Materials for Solid Hydrogen Storage: A Review. *Int. J. Hydrogen Energy* **2007**, *32*, 1121−1140.

(18) Umegaki, T.; Yan, J.-M.; Zhang, X.-B.; Shioyama, H.; Kuriyama, N.; Xu, Q. Boron- and Nitrogen-Based Chemical Hydrogen Storage Materials. *Int. J. Hydrogen Energy* **2009**, *34*, 2303−2311.

(19) Bowman, R. C., Jr.; Reiter, J. W.; Hwang, S.-J.; Kim, C.; Kabbour, H. Characterization of Complex Metal Hydrides by High-Resolution Solid State NMR Spectroscopy. *Mater. Issues Hydrogen Econ.* **2009**, *192*.

(20) Hwang, S.-J.; Bowman, R. C., Jr.; Kim, C.; Zan, J. A.; Reiter, J. W. Solid State NMR Characterization of Complex Metal Hydrides systems for Hydrogen Storage Applications. *J. Anal. Sci. Technol.* **2011**, *2*, A159−A162.

(21) Jepsen, L. H.; Ban, V.; Møller, K. T.; Lee, Y.-S.; Cho, Y. W.; Besenbacher, F.; Filinchuk, Y.; Skibsted, J.; Jensen, T. R. Synthesis, Crystal Structure, Thermal Decomposition, and ^{11}B MAS NMR Characterization of $Mg(BH_4)_2(NH_3BH_3)_2$. *J. Phys. Chem. C* **2014**, *118*, 12141−12153.

(22) Bérubé, V.; Radtke, G.; Dresselhaus, M.; Chen, G. Size Effects on the Hydrogen Storage Properties of Nanostructured Metal Hydrides: A review. *Int. J. Energy Res.* **2007**, *31*, 637−663.

(23) de Jongh, P. E.; Adelhelm, P. Nanosizing and Nanoconfinement: New Strategies Towards Meeting Hydrogen Storage Goals. *ChemSusChem* **2010**, *3*, 1332−1348.

(24) Ngene, P.; van Zwienen, M. R.; de Jongh, P. E. Reversibility of the Hydrogen Desorption from LiBH₄: A Synergetic Effect of Nanoconfinement and Ni Addition. *Chem. Commun.* **2010**, *46*, 8201−8203.

(25) Gutowska, A.; Li, L.; Shin, Y.; Wang, C. M.; Li, X. S.; Linehan, J. C.; Smith, R. S.; Kay, B. D.; Schmid, B.; Shaw, W.; Gutowski, M.; Autrey, T. Nanoscaffold Mediates Hydrogen Release and the Reactivity of Ammonia Borane. *Angew. Chem., Int. Ed.* **2005**, *44*, 3578−3582.

(26) Shane, D. T.; Corey, R. L.; McIntosh, C.; Rayhel, L. H.; Bowman, R. C., Jr.; Vajo, J. J.; Gross, A. F.; Conradi, M. S. LiBH₄ in Carbon Aerogel Nanoscaffolds: An NMR Study of Atomic Motions. *J. Phys. Chem. C* **2010**, *114*, 4008−4014.

(27) Corey, R. L.; Shane, D. T.; Bowman, R. C., Jr.; Conradi, M. S. Atomic Motions in LiBH₄ by NMR. *J. Phys. Chem. C* **2008**, *112*, 18706−18710.

(28) Blanchard, D.; Nale, A.; Sveinbjörnsson, D.; Eggenhuisen, T. M.; Verkuijlen, M. H. W.; Suwarno; Vegge, T.; Kentgens, A. P. M.; de Jongh, P. E. Nanoconfined LiBH₄ as a Fast Lithium Ion Conductor. *Adv. Funct. Mater.* **2015**, *25*, 184−192.

(29) Epp, V.; Wilkening, M. Motion of Li⁺ in Nanoengineered LiBH₄ and LiBH₄:Al₂O₃ Comparison with the Microcrystalline Form. *ChemPhysChem* **2013**, *14*, 3706−3713.

(30) Choi, Y. S.; Lee, Y.-S.; Oh, K. H.; Cho, Y. W. Interface-Enhanced Li Ion Conduction in a LiBH₄-SiO₂ Solid Electrolyte. *Phys. Chem. Chem. Phys.* **2016**, *18*, 22540−22547.

(31) Choi, Y. S.; Lee, Y.-S.; Choi, D.-J.; Chae, K. H.; Oh, K. H.; Cho, Y. W. Enhanced Li Ion Conductivity in LiBH₄-Al₂O₃ Mixture via Interface Engineering. *J. Phys. Chem. C* **2017**, *121*, 26209−26215.

(32) Matsuo, M.; Orimo, S.-i. Lithium Fast-Ionic Conduction in Complex Hydrides: Review and Prospects. *Adv. Energy Mater.* **2011**, *1*, 161−172.

(33) Knauth, P.; Schoonman, J. *Nanocomposites - Ionic Conducting Materials and Structural Spectroscopies*; Springer Science & Business Media: New York, 2007.

(34) Heitjans, P.; Indris, S. Diffusion and Ionic Conduction in Nanocrystalline Ceramics. *J. Phys.: Condes. Matter* **2003**, *676*, Y6.6.

(35) Maier, J. Nano-Ionics: Trivial and Non-Trivial Size Effects on Ion Conduction in Solids. *Z. Phys. Chem.* **2003**, *217*, 415−436.

(36) Breuer, S.; Pregartner, V.; Lunghammer, S.; Wilkening, H. M. R. Dispersed Solid Conductors: Fast Interfacial Li-Ion Dynamics in Nanostructured LiF and LiF:γ-Al₂O₃ Composites. *J. Phys. Chem. C* **2019**, *123*, 5222−5230.

(37) Ardel, G.; Golodnitsky, D.; Peled, E.; Wang, Y.; Wang, G.; Bajue, S.; Greenbaum, S. Bulk and Interfacial Ionic Conduction in LiI/Al₂O₃ Mixtures. *Solid State Ionics* **1998**, *113-115*, 477−485.

(38) Breuer, S.; Uitz, M.; Wilkening, H. M. R. Rapid Li Ion Dynamics in the Interfacial Regions of Nanocrystalline Solids. *J. Phys. Chem. Lett.* **2018**, *9*, 2093−2097.

(39) Prutsch, D.; Breuer, S.; Uitz, M.; Bottke, P.; Langer, J.; Lunghammer, S.; Philipp, M.; Posch, P.; Pregartner, V.; Stanje, B.; Dunst, A.; Wohlmuth, D.; Brandstätter, H.; Schmidt, W.; Epp, V.; Chadwick, A.; Hanzu, I.; Wilkening, M. Nanostructured Ceramics: Ionic Transport and Electrochemical Activity A Short Journey Across Various Families of Materials. *Z. Phys. Chem.* **2017**, *231*, 1361−1405.

(40) Gadermaier, B.; Stanje, B.; Wilkening, A.; Hanzu, I.; Heitjans, P.; Wilkening, H. M. R. Glass in Two Forms: Heterogeneous Electrical Relaxation in Nanoglassy Petalite. *J. Phys. Chem. C* **2019**, *123*, 10153−10162.

(41) Maier, J. Ionic Conduction in Space Charge Regions. *Prog. Solid State Chem.* **1995**, *23*, 171−263.

(42) Maier, J. Space-Charge Regions in Solid 2-Phase Systems and Their Conduction Contribution - Conductance Enhancement in the System Ionic Conductor-'Inert' Phase and Application on AgCl-Al₂O₃ and AgCl-SiO₂. *J. Phys. Chem. Solids* **1985**, *46*, 309−320.

(43) Knauth, P.; Albinet, G.; Debierre, J.-M. Enhanced Electrical Conductivity of CuBr-TiO₂ Composites: Dependence on Temperature, Volume Fractions and Grain Sizes. *Ber. Bunsenges. Phys. Chem.* **1998**, *102*, 945−952.

(44) Verkuijlen, M. H. W.; Ngene, P.; de Kort, D. W.; Barré, C.; Nale, A.; van Eck, E. R. H.; van Bentum, P. J. M.; de Jongh, P. E.; Kentgens, A. P. M. Nanoconfined LiBH₄ and Enhanced Mobility of Li⁺ and BH₄⁻ Studied by Solid-State NMR. *J. Phys. Chem. C* **2012**, *116*, 22169−22178.

(45) Lefevr, J.; Cervini, L.; Griffin, J. M.; Blanchard, D. Lithium Conductivity and Ions Dynamics in LiBH₄/SiO₂ Solid Electrolytes Studied by Solid-State NMR and Quasi-Elastic Neutron Scattering and Applied in Lithium Sulfur Batteries. *J. Phys. Chem. C* **2018**, *122*, 15264−15275.

(46) Lambregts, S. F. H.; van Eck, E. R. H.; Suwarno; Ngene, P.; de Jongh, P. E.; Kentgens, A. P. M. Phase Behavior and Ion Dynamics of Nanoconfined LiBH₄ in Silica. *J. Phys. Chem. C* **2019**, *123*, 25559−25569.

(47) Maekawa, H.; Matsuo, M.; Takamura, H.; Ando, M.; Noda, Y.; Karahashi, T.; Orimo, S.-i. Halide-Stabilized LiBH₄, a Room-Temperature Lithium Fast-Ion Conductor. *J. Am. Chem. Soc.* **2009**, *131*, 894−895.

(48) Matsuo, M.; Remhof, A.; Martelli, P.; Caputo, R.; Ernst, M.; Miura, Y.; Sato, T.; Oguchi, H.; Maekawa, H.; Takamura, H.; Borgschulte, A.; Züttel, A.; Orimo, S.-i. Complex Hydrides with BH₄⁻ and NH₂⁻ Anions as New Lithium Fast-Ion Conductors. *J. Am. Chem. Soc.* **2009**, *131*, 16389−16391.

(49) Gulino, V.; Barberis, L.; Ngene, P.; Baricco, M.; de Jongh, P. E. Enhancing Li-Ion Conductivity in LiBH₄-Based Solid Electrolytes by Adding Various Nanosized Oxides. *ACS Appl. Energy Mater.* **2020**, *3*, 4941−4948.

(50) Kwak, J. H.; Hu, J. Z.; Kim, D. H.; Szanyi, J.; Peden, C. H. F. Pentacoordinated Al³⁺ Ions as Preferential Nucleation Sites for BaO on γ-Al₂O₃: An Ultra-High-Magnetic field ²⁷Al MAS NMR study. *J. Catal.* **2007**, *251*, 189−194.

(51) Kwak, J. H.; Hu, J.; Lukaski, A.; Kim, D. H.; Szanyi, J.; Peden, C. H. F. Role of Pentacoordinated Al³⁺ Ions in the High Temperature Phase Transformation of γ-Al₂O₃. *J. Phys. Chem. C* **2008**, *112*, 9486−9492.

(52) Düvel, A.; Romanova, E.; Sharifi, M.; Freude, D.; Wark, M.; Heitjans, P.; Wilkening, M. Mechanically Induced Phase Transformation of γ-Al₂O₃ into α-Al₂O₃: Access to Structurally Disordered γ-Al₂O₃ with a Controllable Amount of Pentacoordinated Al Sites. *J. Phys. Chem. C* **2011**, *115*, 22770−22780.

(53) Suwarno; Ngene, P.; Nale, A.; Eggenhuisen, T. M.; Oschatz, M.; Embs, J. P.; Remhof, A.; de Jongh, P. E. Confinement Effects for Lithium Borohydride: Comparing Silica and Carbon Scaffolds. *J. Phys. Chem. C* **2017**, *121*, 4197−4205.

(54) Shane, D. NMR Study of Borohydrides for Hydrogen Storage Applications. Dissertation, Washington University in St. Louis, 2011.

(55) Senadheera, L.; Carl, E. M.; Ivancic, T. M.; Conradi, M. S.; Bowman, R. C., Jr.; Hwang, S.-J.; Udovic, T. J. Molecular H₂ trapped in AlH₃ solid. *J. Alloys Compd.* **2008**, *463*, 1−5.

(56) Hwang, S.-J.; Bowman, R. C.; Reiter, J. W.; Rijssenbeek; Soloveichik, G. L.; Zhao, J.-C.; Kabbour, H.; Ahn, C. C. NMR Confirmation for formation of [B₁₂H₁₂]²⁻ Complexes During Hydrogen Desorption from Metal Borohydrides. *J. Phys. Chem. C* **2008**, *112*, 3164−3169.

(57) Epp, V.; Wilkening, M. Fast Li Diffusion in Crystalline LiBH₄ due to Reduced Dimensionality: Frequency-Dependent NMR Spectroscopy. *Phys. Rev. B* **2010**, *82*, No. 020301.

(58) Jonscher, A. K. The 'Universal' Dielectric Response. *Nature* **1977**, *267*, 673−679.

(59) Sidebottom, D. L. Dimensionality Dependence of the Conductivity Dispersion in Ionic Materials. *Phys. Rev. Lett.* **1999**, *83*, 983−986.

(60) Matsuo, M.; Nakamori, Y.; Orimo, S.-i.; Maekawa, H.; Takamura, H. Lithium Superionic Conduction in Lithium Borohydride Accompanied by Structural Transition. *Appl. Phys. Lett.* **2007**, *91*, 224103.

(61) Aeberhard, P. C.; Williams, S. R.; Evans, D. J.; Refson, K.; David, W. I. F. Ab initio Nonequilibrium Molecular Dynamics in the

Solid Superionic Conductor LiBH$_4$. *Phys. Rev. Lett.* **2012**, *108*, 095901.

(62) Myrdal, J. S. G.; Blanchard, D.; Sveinbjörnsson, D.; Vegge, T. Li-ion Conduction in the LiBH$_4$:LiI System from Density Functional Theory Calculations and Quasi-Elastic Neutron Scattering. *J. Phys. Chem. C* **2013**, *117*, 9084−9091.

(63) Preishuber-Pflügl, F.; Bottke, P.; Pregartner, V.; Bitschnau, B.; Wilkening, M. Correlated Fluorine Diffusion and Ionic Conduction in the Nanocrystalline F$^-$ Solid Electrolyte Ba$_{0.6}$La$_{0.4}$F$_{2.4}$ - ^{19}F $T_{1\rho}$ NMR Relaxation vs. Conductivity Measurements. *Phys. Chem. Chem. Phys.* **2014**, *16*, 9580−9590.

(64) Wilkening, M.; Heitjans, P. Li jump Process in *h*-Li$_{0.7}$TiS$_2$ Studied by Two-Time ^{7}Li Spin-Alignment Echo NMR and Comparison with Results on Two-Dimensional Diffusion from nuclear Magnetic Relaxation. *Phys. Rev. B* **2008**, *77*, No. 024311.

(65) Wilkening, M.; Indris, S.; Heitjans, P. Heterogeneous Lithium Diffusion in Nanocrystalline Li$_2$O:Al$_2$O$_3$ Composites. *Phys. Chem. Chem. Phys.* **2003**, *5*, 2225−2231.

(66) Wilkening, M.; Heitjans, P. From Micro to Macro: Access to Long-Range Li$^+$ Diffusion Parameters in Solids via Microscopic ^{6}Li, ^{7}Li Spin-Alignment Echo NMR Spectroscopy. *ChemPhysChem* **2012**, *13*, 53−65.

(67) Winter, R.; Heitjans, P. Li$^+$ Diffusion and its Structural Basis in the Nanocrystalline and Amorphous Forms of Two-Dimensionally Ion-Conducting Li$_x$TiS$_2$. *J. Phys. Chem. B* **2001**, *105*, 6108−6115.

(68) Liu, X.; Majzoub, E. H.; Stavila, V.; Bhakta, R. K.; Allendorf, M. D.; Shane, D. T.; Conradi, M. S.; Verdal, N.; Udovic, T. J.; Hwang, S.-J. Probing the Unusual Anion Mobility of LiBH$_4$ Confined in Highly Ordered Nanoporous Carbon Frameworks via Solid State NMR and Quasielastic Neutron Scattering. *J. Mater. Chem. A* **2013**, *1*, 9935−9941.

(69) Sata, N.; Eberman, K.; Eberl, K.; Maier, J. Mesoscopic Fast Ion Conduction in Nanometre-Scale Planar Heterostructures. *Nature* **2000**, *408*, 946−949.

(70) Maier, J. Nanoionics: Ion Transport and Electrochemical Storage in Confined Systems. *Nat. Mater.* **2005**, *4*, 805−815.